Current Optics and Photonics
Vol. 3, No. 5, October 2019, pp. 445-450

ISSN: 2508-7266(Print) / ISSN: 2508-7274(Online)
DOI: https://doi.org/10.3807/COPP.2019.3.5.445

Influence of Emitter Width on the Performance of 975-nm (In,Ga)(As,P)/(Al,Ga)As High-power Laser Diodes

Jung-Tack Yang[1], Younghyun Kim[2], Marzieh Pournoury[2], Jae-Bong Lee[3], Dong-Soo Bang[3], Tae-Kyung Kim[3], and Woo-Young Choi[1]*

[1]*Department of Electrical and Electronic Engineering, Yonsei University, Seoul 03722, Korea*
[2]*Formerly at Department of Electrical and Electronic Engineering, Yonsei University, Seoul 03722, Korea*
[3]*QSI, Cheonan 31044, Korea*

(Received June 3, 2019 : revised August 5, 2019 : accepted August 5, 2019)

The influence of high-power laser diode (HPLD) emitter width on the device performance is investigated for 975-nm (In,Ga)(As,P)/(Al,Ga)As broad-area HPLDs, using self-consistent electro-thermal-optical simulation. To guarantee the simulation's accuracy, simulated results are matched with the measured results for a sample HPLD with fitting parameters. The influences of HPLD emitter width on temperature distribution, output power, and the beam product parameter (BPP) are analyzed for three different emitter widths of 50, 70, and 90 μm. It is found that a device with smaller emitter width exhibits both thermal rollover and thermal blooming at lower output power, but smaller BPP.

Keywords : High-power laser diode, Thermal roll-over, Thermal blooming, Emitter width
OCIS codes : (140.2020) Diode lasers; (140.5960) Semiconductor lasers

I. INTRODUCTION

Yb-doped fiber lasers play an important role in a wide range of applications in micromachining, medicine, the military, and communication [1, 2]. To achieve the best performance in terms of fiber-laser output power and efficiency, the use of good-quality pumping sources is essential [3]. With high power-conversion efficiency (PCE), small size, and mass-production capability, high-power laser diodes (HPLDs) are the pumping source of choice [4-6]. 975-nm HPLDs realized on GaAs substrates have attracted much research and development effort for Yb-doped fiber laser applications.

In HPLDs, device performance is often limited by thermal rollover and thermal blooming. With high injection currents the device temperature rises, and eventually the output optical power decreases with increasing current, resulting in thermal rollover. In addition, HPLDs often suffer from thermal blooming, the widening of the lateral far field, with high injection currents. The nonuniform lateral temperature profile from the center to the edge of the device causes stronger guidance for the lateral waveguide, resulting in the wider far-field pattern [7, 8]. It is very important to have a clear understanding of these thermal problems, to achieve optimal HPLD performance. For this, numerical analysis of the interaction between electronic, optical, and thermal processes in HPLDs can be an important analysis technique. In this paper we investigate how the emitter width influences various performance aspects of 975-nm HPLDs with LASTIP [9], a commercially available self-consistent electro-thermal-optical two-dimensional laser simulator.

This paper is organized as follows. In Section 2, we introduce our 975-nm HPLD device's structure, and verify the accuracy of our simulation with measured results. In Sections 3 and 4, we analyze the dependence of the 975-nm HPLD's output power and beam product parameter (BPP) performance on emitter width. In Section 5, we conclude the paper.

*Corresponding author: wchoi@yonsei.ac.kr, ORCID 0000-0003-0067-4657
Color versions of one or more of the figures in this paper are available online.

II. DEVICE STRUCTURE AND FITTING-PARAMETER EXTRACTION

Figure 1(a) shows the device structure of the 975-nm HPLD investigated in this study. The band diagram from the top layer to the substrate is shown in Fig. 1(b). The active region contains one 15-nm-thick (In,Ga)(As,P) quantum well (QW) under compressive strain plus undoped (Al,Ga)As asymmetric barrier/waveguide layers. A current-blocking barrier (CBB) is added inside the bottom waveguide layer. The *n*- and *p*-type cladding layers are highly doped (Al,Ga)As layers having higher Al mole fraction than the waveguide layers. SiN is used as the insulator material next to the ridge structure. Both the *p*-type cap and *n*-type buffer layers consist of very highly doped GaAs layers.

The first task in performing HPLD analysis with simulation is establishing the accuracy of the simulated results. For this, a 975-nm HPLD device having 90-μm emitter width, a 4-mm-long cavity, and facet reflectivities of 1% and 99% is fabricated, and its *I-V* and *L-I* characteristics are measured. The results are shown in Figs. 2(a) and 2(b). The inset in Fig. 2(a) shows the measured slope efficiencies at different injection currents. For the measurements, currents ranging from 0 to 14 A are injected into the device, which is placed in a package with a passive heat sink. The laser power is measured by collecting the laser output into an integrating sphere with a calibrated photodetector.

The *I-V* and *L-I* characteristics of the target HPLD are simulated in LASTIP. To achieve accurate simulation results, accurate parameter values should be available for temperature-dependent nonradiative recombination processes such as Shockley-Read-Hall (SRH) recombination, Auger recombination, and temperature-dependent internal loss. However, these are not readily available, and their direct measurement is very complicated. Instead, their values are determined with a numerical fitting process in this investigation.

For the two nonradiative recombination processes here, SRH recombination is dominant when the injected current is small, and Auger recombination when the injected current is large. This is because the former is proportional to the injected carrier density, while the latter is proportional to the cube of the injected carrier density. With this knowledge, the SRH recombination rate is used initially to fit the simulated threshold current to the measured result. Then

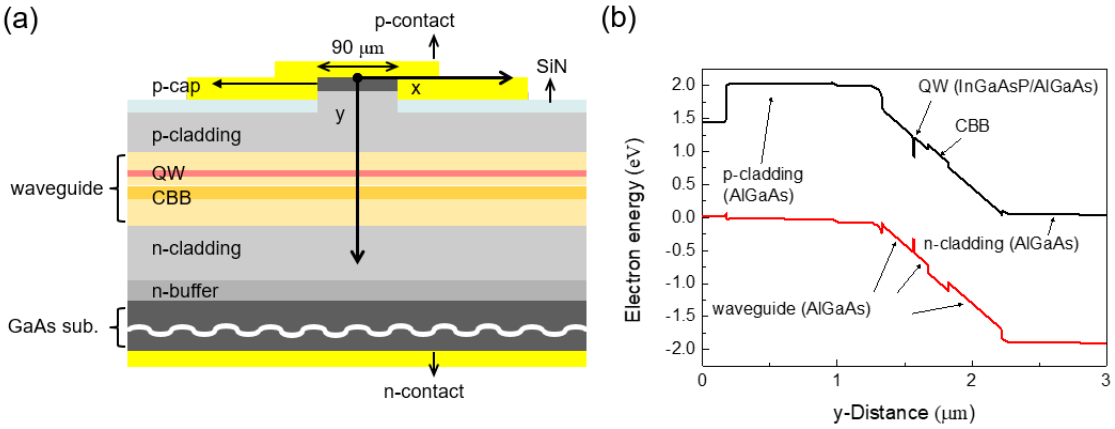

FIG. 1. Device structure of the 975-nm HPLD: (a) Cross section, (b) Band diagram.

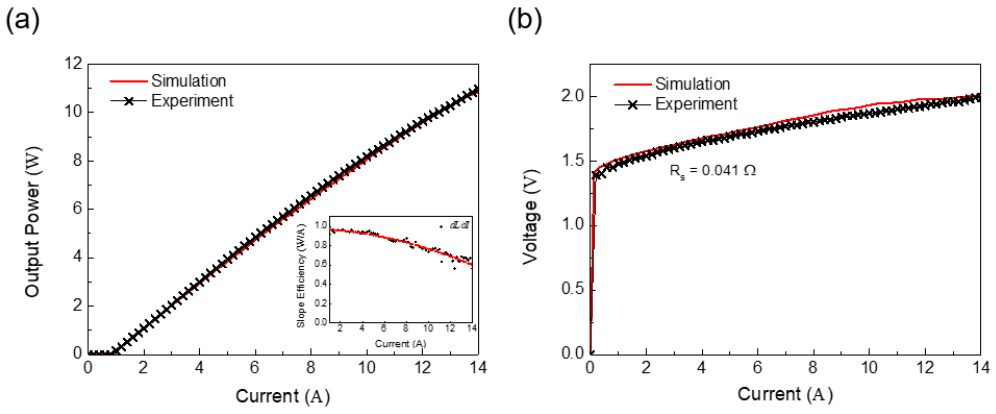

FIG. 2. Measured and simulated results: (a) *L-I* curve, (b) *V-I* curve.

the Auger recombination is used to fit the simulated slope efficiency, and the thermal rollover for high injected current, to the measurement results. For SRH recombination, the temperature-dependent lifetime $\tau(T)$ is given as [11]

$$\tau(T) = \tau_0 \times \left(\frac{T}{298}\right)^{\gamma}, \quad (1)$$

where τ_0 and γ are fitting parameters. The Auger recombination rate is modeled with $C(n+p)(np-n_i^2)$, where n, p, and n_i represent the electron, hole, and intrinsic carrier concentrations respectively, and C is a coefficient whose temperature dependence is described by [12]

$$C(T) = C_0 \times \exp\left[\frac{E_A}{k}\left(\frac{1}{298} - \frac{1}{T}\right)\right], \quad (2)$$

where k is Boltzmann's constant, the activation energy E_A is taken to be 100 meV, and C_0 is a fitting parameter. In addition, fine tuning of the slope of the *L-I* curve is achieved by using the linear-temperature-dependent internal loss [13] given as

$$\alpha_i(T) = \alpha_0 + \beta(T - 298). \quad (3)$$

For good matching, $\tau_0 = 6\times10^{-9}$ s, γ = -3.5, $C_0 = 5\times10^{-29}$ cm^6s^{-1}, $\alpha_0 = 1.8$ cm^{-1}, and $\beta = 0.03$ $K^{-1}cm^{-1}$ are used. In addition, for our simulation it was important to set the correct thermal boundary conditions. Figure 3 shows the thermal boundary conditions used in our simulation. Our simulator, LASTIP, has three options for thermal boundaries: In the first option, the boundary is assumed to be a heat sink. In the second option, the boundary is assumed to have the specified outgoing heat flux. In the third option, the boundary is assumed to be connected to a thermal conductor with the specified thermal conductance. For our simulation, we applied the second option for the bottom *n*-type contact, with zero outgoing heat flux, which means that the substrate is thick enough so that the bottom temperature of the substrate remains at room temperature (298 K). For the top *p*-type contact, we applied the third option with a thermal conductance per unit length of 6000 W/mK, which is calculated from the thermal conductivity (57 W/mK) of AuSn solder that has a width of 480 μm and thickness of 4.6 μm, with the assumption that the top heat sink's temperature remains at room temperature.

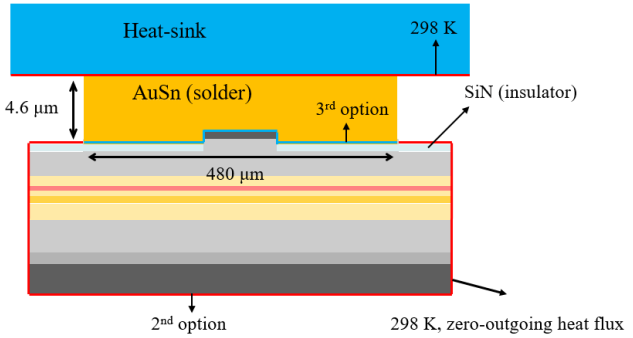

FIG. 3. Cross section showing the thermal boundary conditions.

As Figs. 2(a) and 2(b) show, good matching between measured and simulated results is achieved for both *L-I* and *I-V* characteristics. Our HPLD has a threshold current of about 800 mA and maximum slope efficiency of 0.97 W/A at 2.2 A, and a minimum of 0.565 W/A at 12 A, with the value of *dL/dI* decreasing almost quadratically (Fig. 2(a)). The series resistance is 0.041 Ω, the maximum PCE is about 45%, threshold loss is 11.2%, Joule loss is 16.5%, and other losses are 27.3%. The simulation of our HPLD devices requires about 4 hours on a Windows server with an 8-core i7-7820X CPU and 128 GB of memory.

III. *L-I* CHARACTERISTICS AND THERMAL ROLLOVER

With the accuracy of our HPLD simulation established, the influence of various HPLD structures on HPLD performance can be investigated before actual devices are fabricated. In particular, we are interested in characterizing the influence of the HPLD emitter width L on HPLD thermal properties and BPP. Three different devices with emitter widths of 50, 70, and 90 μm are investigated, with the fixed fill factor defined as the ratio of emitter width to total device width.

Figure 4(a) shows the simulated *L-I* characteristics and PCEs for HPLDs with different emitter widths. Devices with emitter widths of $L = 50$, 70, and 90 μm have threshold currents of about 500, 600, and 800 mA respectively. The maximum output powers are about 8.6, 12, and 14.5 W respectively, before thermal rollover is reached. We can observe that the $L = 50$ μm device suffers from thermal rollover at the lowest injected current, and its PCE drops more rapidly than other devices. This is because the $L =$ 50 μm device has higher temperature rise, due to smaller emitter width and the resulting higher series resistance, as can be seen in Fig. 4(b), which shows the simulated QW temperature for each device as a function of injected current.

Figures 5(a), 5(b), and 5(c) show the two-dimensional temperature profiles for three devices when the injected current is 8 A, for which the $L = 50$ μm device starts to show thermal degradation. All devices have a similar temperature distribution pattern, in which the highest temperature is reached in the center of the device. Figure 5(d) shows the temperature distribution at the center of the device along the y direction. As can be seen in the figure, the $L = 50$ μm device has the highest temperature as well as the largest temperature difference between center and edge.

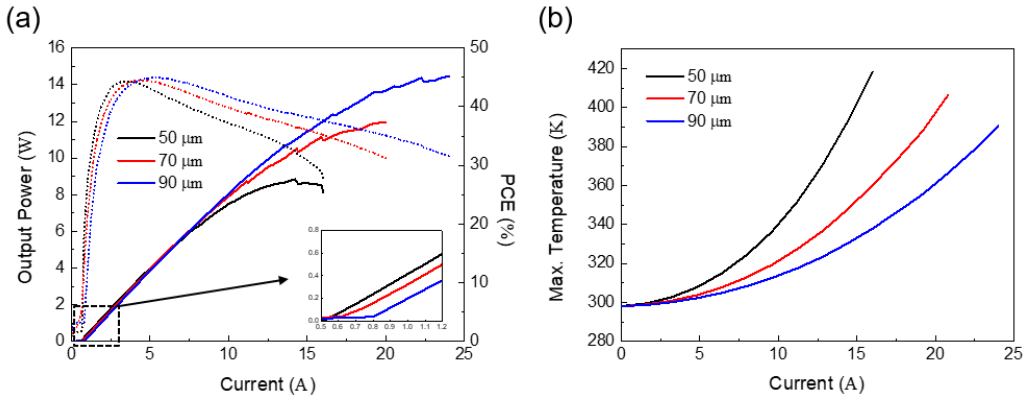

FIG. 4. (a) *L-I* curve and PCE for each emitter width (50, 70, and 90 μm) by driving current, (b) Maximum temperature in the QW for each emitter width.

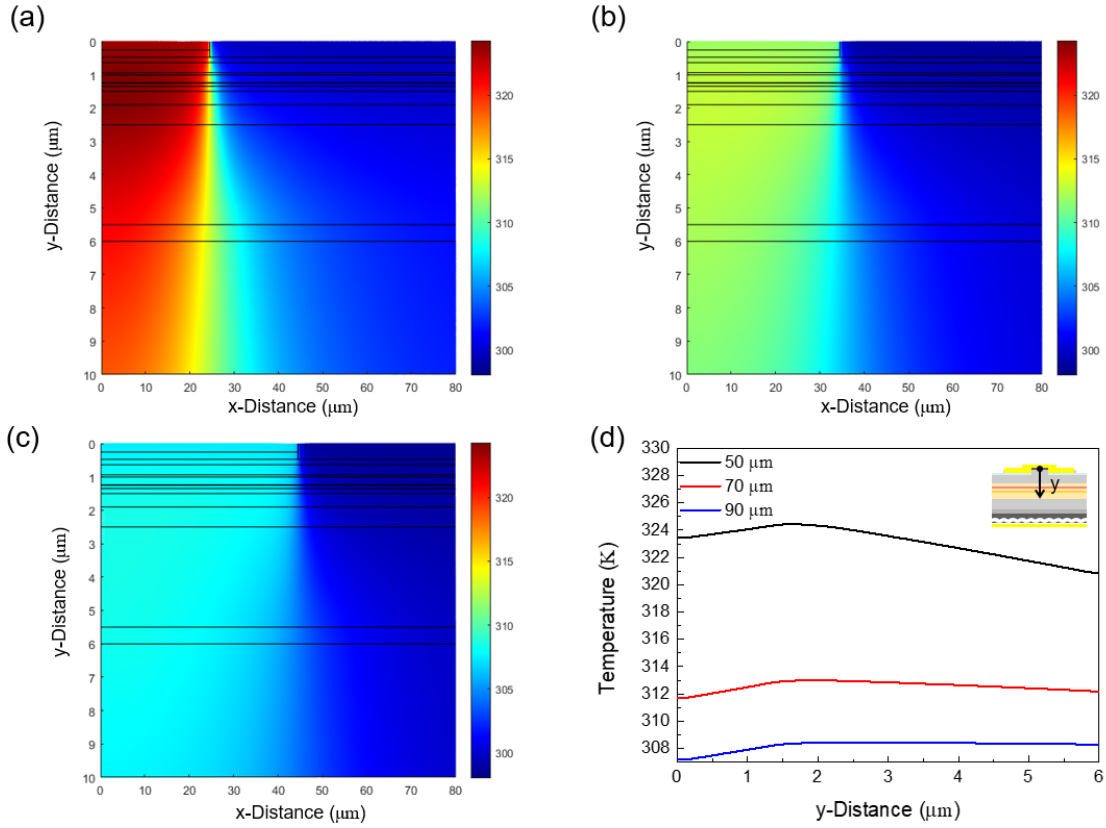

FIG. 5. Temperature distribution along the *x* and *y* directions (as shown in Fig. 1(a)) for emitter width of (a) 50 μm, (b) 70 μm, and (c) 90 μm, at 8 A; and (d) temperature distribution along the *y* direction.

IV. BPP AND THERMAL BLOOMING

Figure 6(a) shows the temperature (solid lines) and refractive-index (dashed lines) distributions of the device with $L = 90$ μm along the *x* direction, at output powers of 3.7 and 12 W. At the higher output power, there is larger difference between center and edge temperatures, resulting in a larger difference in refractive indices. Consequently, the lateral wave confinement becomes stronger, resulting in the thermal lensing effect, and more lateral guided modes are produced. Specifically, there are 15 lateral modes for output power of 3.7 W, whereas there are 49 modes for 12 W. These differences in the lateral mode number results in the difference in the far-field patterns. As can be seen in Fig. 6(b), the HPLD with higher output power has the wider far-field pattern, or suffers from thermal blooming.

Figure 7(a) shows for each device the BPP, defined as the product of the half-waist of the near-field pattern and

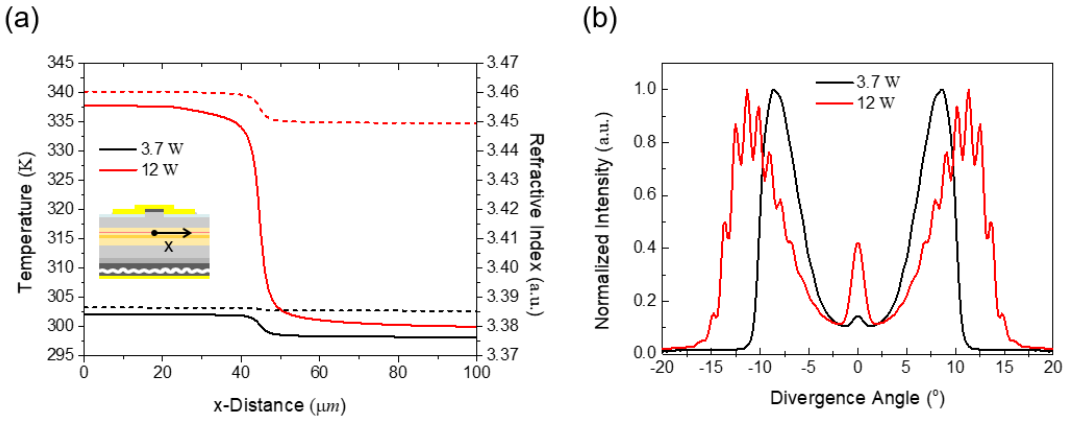

FIG. 6. (a) Temperature (solid lines) and refractive-index (dashed lines) distributions along the *x* direction. (b) Far-field patterns at 3.7 and 12 W for $L = 90$ μm.

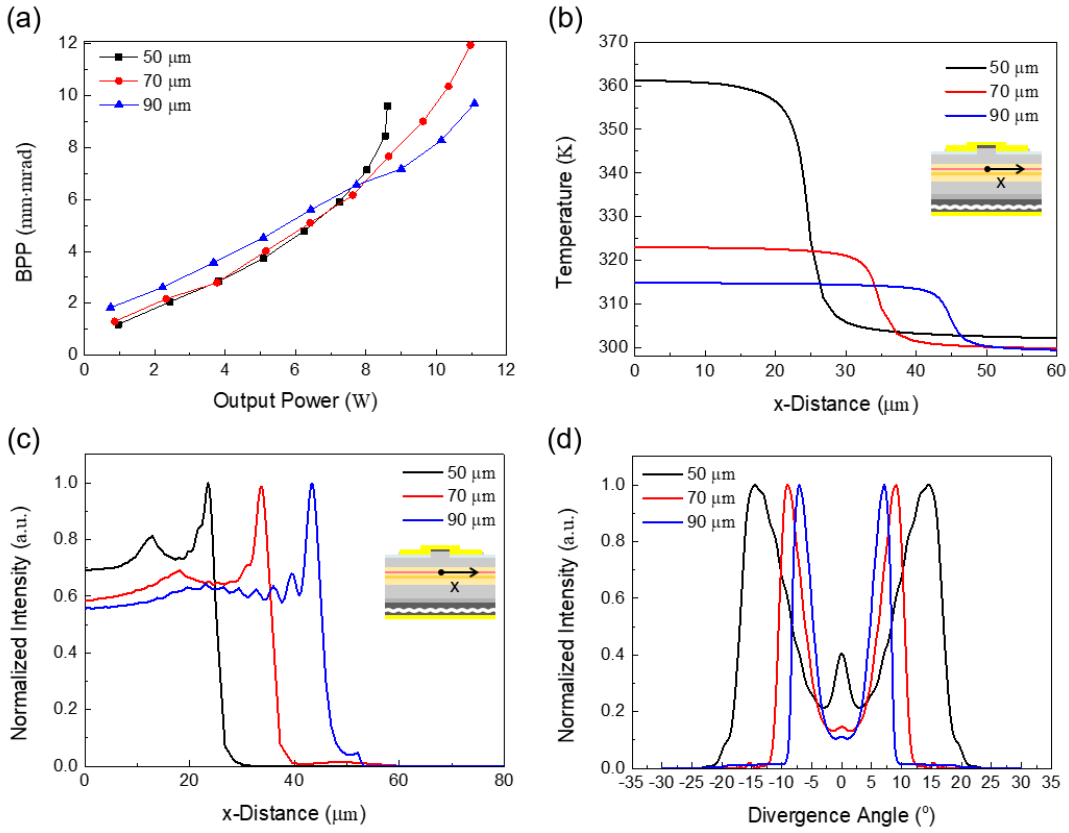

FIG. 7. (a) Calculated BPP and (b) temperature distribution in the active region along the *x* direction (see Fig. 1(a)); (c) near-field pattern and (d) far-field pattern at 8.2 W, for emitter widths of 50, 70, and 90 μm.

the half-angle of the far-field pattern [14], as well as the total number of supported lateral modes as a function of output power. As can be seen in the figure, both BPP and lateral mode number increase with increasing output power, and the increase is most rapid for the device with the smallest emitter width. At low output power, the device with emitter width of $L = 50$ μm has the smallest BPP, but at higher output power its BPP becomes the largest. Figure 7(b) shows the temperature distribution in the active region of each device in the *x* direction, at an output power of 8.2 W. The temperature differences between center and edge are 59.3, 23.6, and 16 K for emitter widths of $L = 50$, 70, and 90 μm respectively. Consequently, the device with $L = 50$ μm suffers from thermal blooming and lensing most significantly. The near- and far-field patterns are shown for each device in Figs. 7(c) and 7(d). The near-field pattern's

waist is almost the same as the emitter width, but there is a significant difference in far-field profiles due to the thermal lensing effect.

V. CONCLUSION

A two-dimensional self-consistent electro-thermal-optical simulation is performed to investigate the influence of emitter width on the performance of a 975-nm HPLD. *L-I* characteristics as well as temperature distributions at different emitter widths are simulated, after careful calibration of simulated results with measured results. It is found that a device with smaller emitter width exhibits both thermal rollover and thermal blooming at lower output power, but smaller BPP.

ACKNOWLEDGMENT

This work was supported by the Research Fund of High Efficiency Laser Laboratory of Agency for Defense Development of Korea (No. UD160069BD).

REFERENCES

1. Y. Jeong, J. K. Sahu, D. N. Payne, and J. Nilsson, "Ytterbium-doped large-core fiber laser with 1 kW continuous-wave output power," in *Proc. Advanced Solid-State Photonics 2004* (Optical Society of America, New Mexico, US, 2004), paper PDP13.
2. Y. Jeong, J. K. Sahu, D. N. Payne, and J. Nilsson, "Ytterbium-doped large-core fiber laser with 1.36 kW continuous-wave output power," Opt. Express **12** 6088-6092 (2004).
3. A. Liu, M. A. Norsen, and R. D. Mead, "60-W green output by frequency doubling of a polarized Yb-doped fiber laser," Opt. Lett. **30**, 67-69 (2005).
4. L. Zhong and X. Ma, "Recent developments in high power semiconductor diode lasers," in *Optoelectronics - Devices and Applications*, P. Predeep, ed. (InTech, London, UK, 2011), Chapter 16, pp. 325-348.
5. V. Gapontsev, N. Moshegov, I. Berezin, A. Komissarov, P. Trubenko, D. Miftakhutdinov, I. Berishev, V. Chuyanov, O. Raisky, and A. Ovtchinnikov, "Highly-efficient high-power pumps for fiber lasers," Proc. SPIE **10086**, 1008604 (2017).
6. A. V. Aluev, A. M. Morozyuk, M. S. Kobyakova, and A. A. Chel'nyi, "High-power 2.5-W cw AlGaAs/GaAs laser diodes," Quantum Electron. **31**, 627-628 (2001).
7. J. Piprek, "Self-consistent far-field blooming analysis for high-power Fabry-Perot laser diodes," Proc. SPIE **8619**, 861910 (2013).
8. P. Crump, S. Bldicke, C. M. Schultz, H. Ekhteraei, H. Wenzel, and G. Erbert, "Experimental and theoretical analysis of the dominant lateral waveguiding mechanism in 975 nm high power broad area diode lasers," Semicond. Sci. Technol. **27**, 045001 (2012).
9. PICS3D, Crosslight Software Inc. [Online]. Available: http://www. crosslight.com (2016).
10. S.-S. Beyertt, M. Zorn, T. Kübler, H. Wenzel, M. Weyers, A. Giesen, G. Tränkle, and U. Brauch, "Optical in-well pumping of a semiconductor disk laser with high optical efficiency," IEEE J. Quantum Electron. **41**, 1439-1449 (2005).
11. C. J. Hages, A. Redinger, S. Levcenko, H. Hempel, M. J. Koeper, R. Agrawal, D. Greiner, C. A. Kaufmann, and T. Unold, "Identifying the real minority carrier lifetime in nonideal semiconductors: a case study of kesterite materials," Adv. Energy Mater. **7**, 1700167 (2017).
12. J. Piprek, J. K. White, and A. J. SpringThorpe, "What limits the maximum output power of long-wavelength AlGaInAs/InP laser diodes?," IEEE J. Quantum Electron. **38**, 1253-1259 (2002).
13. N. A. Pikhtin, S. O. Slipchenko, I. S. Shashkin, M. A. Ladugin, A. A. Marmalyuk, A. A. Podoskin, and I. S. Tarasov, "The temperature dependence of internal optical losses in semiconductor lasers (λ = 900-920 nm)," Semiconductors **44**, 1365-1369 (2010).
14. A. Bachmann, C. Lauer, M. Furitsch, H. Knig, M. Mller, and U. Strau, "Recent brightness improvements of 976 nm high power laser bars," Proc. SPIE **10086**, 1008602 (2017).